

This is the peer reviewed version of the following article: An, Y. M., Long, X., Ma, M., Hu, J., Lin, H., Zhou, D., Xing, Z., Huang, B. L., Yang, S. H., One-Step Controllable Synthesis of Catalytic Ni₄Mo/MoO_x/Cu Nanointerfaces for Highly Efficient Water Reduction. *Adv. Energy Mater.* 2019, 9, 1901454, which has been published in final form at <https://doi.org/10.1002/aenm.201901454>. This article may be used for non-commercial purposes in accordance with Wiley Terms and Conditions for Use of Self-Archived Versions. This article may not be enhanced, enriched or otherwise transformed into a derivative work, without express permission from Wiley or by statutory rights under applicable legislation. Copyright notices must not be removed, obscured or modified. The article must be linked to Wiley's version of record on Wiley Online Library and any embedding, framing or otherwise making available the article or pages thereof by third parties from platforms, services and websites other than Wiley Online Library must be prohibited.

One-step controllable synthesis of Ni₄Mo/MoO_x/Cu nanointerfaces for highly efficient water reduction

Yiming An, Xia Long, Ming Ma, Jue Hu, He Lin, Dan Zhou, Zheng Xing, Bolong Huang, Shihe Yang**

Y. M. An, Dr. X. Long, Dr. M. Ma, Dr. J. Hu, H. Lin, D. Zhou, Dr. Z. Xing, Prof. S. H. Yang
Department of Chemistry
The Hong Kong University of Science and Technology
Clear Water Bay, Kowloon, Hong Kong, China
E-mail: chsyang@ust.hk
Dr. X. Long, Prof. S. H. Yang
Guangdong Key Lab of Nano-Micro Material Research
School of Chemical Biology and Biotechnology Shenzhen Graduate School
Peking University, Shenzhen, China
Prof. B. L. Huang
Department of Applied Biology and Chemical Technology
The Hong Kong Polytechnic University
Hung Hom, Kowloon, Hong Kong, China
E-mail: bhuang@polyu.edu.hk

Keywords: nanointerface, one-step synthesis, d-band structure, NiMo, hydrogen evolution reaction

Currently, besides discovering non-noble metal water-splitting electrocatalysts with intrinsic catalytic activity, the scalable synthetic route and simple activity enhancement strategy are also urgently needed. In particular, the well-control synthesis of the well-recognized metal-metal nanointerfaces a facile fashion, ideally in a single step, remains a key challenge. Here, we report the synthesis of Cu-supported Ni₄Mo nanodot on MoO_x nanosheet (Ni₄Mo/MoO_x) with controllable Ni₄Mo particle size and d-band structure via a facile one-step electrodeposition process. Density functional theory (DFT) calculations reveal the active open-shell effect from Ni-3d-band that reserves an optimal electronic configuration. The support of Cu-substrate turns the surface Ni-Mo alloy dots to be even more electron-rich forming the local connected electron-rich network, which further boosts-up the efficient charge transfer for effective binding of the O-related species and proton-electron charge exchange in HER process. The Cu-supported Ni₄Mo/MoO_x shows an ultra-low overpotential of 16 mV at the current density of 10 mA/cm² in 1 M KOH, demonstrating the smallest overpotential at loading as low as 0.27

mg/cm² among non-noble metal catalysts reported to date. More importantly, an overpotential of 105 mV allows it to achieve a current density of 2500 A/m² in 70 °C 30% KOH, a remarkable performance toward alkaline hydrogen evolution with high potential for commercialization.

Global warming, environmental pollution, and energy shortage have increasingly been regarded as top challenging issues facing humanity in connection with the current reliance on fossil fuels.^[1] Hydrogen (H₂) is widely considered as a promising alternative to fossil fuels with the merits of high gravimetric energy density, high abundance and zero emission.^[2] Water splitting by electrocatalysis is especially attractive with input of electricity and water, and output of high purity H₂.^[3] Though the benchmark electrocatalysts for hydrogen evolution reaction (HER), i.e. Pt-based materials,^[4] require only low electricity input, the scarcity and high cost are discrepant with the economic criteria and considerations.^[5] Thus, robust yet low-cost electrocatalysts are highly desired for efficient hydrogen production, especially in alkaline solution in order to be favorably coupled with the other more sluggish half reaction oxygen evolution reaction (OER).^[6]

Activity, synthetic route, and cost are the main factors determining the widespread industrial applications of electrocatalysts.^[7] Notably, Nickel (Ni) has already been employed for water reduction in industry, however, its apparent shortcomings of large overpotential and Tafel slope demand a much higher energy input than with the noble-metal catalysts for the production of a given H₂ equivalent.^[8] Metal/ metal oxide nanointerface has been proved to possess higher activity than metal alone, however, current methods for fabricating the nanointerfaces commonly involve multiple steps of precursor growth and calcination in reducing atmosphere, which, aside from the imprecise control of the nanointerfaces, suffer from the manufactural complexity.^[8a, 9] Thus, one of the most critical challenges in this regard is to construct the metal/metal oxide nanointerfaces via a facile synthetic route. And a low mass-loading is

expected at the same time to reduce the total cost. Among various hetero-atoms, Mo shows a distinctive synergetic effect with Ni in catalyzing the water reduction reaction.^[10] Interestingly, Mo oxides, albeit distinct from the metallic catalysts such as the ones mentioned above, are also HER active.^[11] Thus, we are inspired to combine NiMo and Mo oxide with noble-metal-like catalytic properties, ideally with a simple and scalable method to replace the current catalysts. We obtain the highly desired NiMo/Mo oxide nanointerfaces by designing the electrodeposition condition to selectively reduce the elements on demand while keeping both the oxide and the metal parts separated by the nanointerfaces. As a matter of fact, global efforts have recently been made to develop such NiMo-based catalysts.^[9a, 9d, 12] Thus far, high performance and simple synthesis of these catalysts have been demonstrated one way or another as a proof of principle, however, real applications on the industrial scale call for assembling a highly active catalyst in place, ideally via a simple one-step synthetic route in order to make it commercially viable.

Herein, we report the synthesis of Cu-supported Ni₄Mo nanodot on MoO_x nanosheet catalyst (Ni₄Mo/MoO_x) with controllable Ni₄Mo particle size and d-band structure via a one-step electrodeposition process, the one which is widely used in the industry. Significantly, we were able to finely tailor the d-band structure of the catalyst by simply taking Cu as the substrate, and optimize the reaction route by elaborating the Ni₄Mo/MoO_x nanointerfaces. In alkaline media, the Cu-supported Ni₄Mo/MoO_x shows an overpotential as small as 16 mV at the current density of 10 mA/cm² with a catalyst loading of only 0.27 mg/cm², which is 0.6% mass loading of previously reported NiMo/oxide materials with comparable activities, beneficial from the substrate effect. Additionally, under typical industrial water electrolysis condition (70 °C, 30% KOH), 105 mV is needed for Ni₄Mo/MoO_x to achieve a current density of 2500 A/m², which stands as one of the most active catalysts toward alkaline hydrogen evolution.

We synthesized the Ni₄Mo nanodot/MoO_x nanosheet structure via a one-step electrodeposition process as shown in **Figure 1A**. In electrodeposition, factors including electrolyte concentration, pH and mass transport, etc. can have a strong impact on the final product. Thus, these factors need to be taken into consideration when finding balance with deposition potential (Details about the mechanism are discussed in supporting information). In the electrodeposition process, the MoO₄²⁻ anions, Ni²⁺ cations, and the citrate anions tend to form [(NiCit)(MoO_x)]⁻_{ads} after an electron transfer process, followed by the reduction of Ni²⁺ to metallic Ni⁰.^[13] (**Figure S1**) This is the crucial process that manifests the striking importance of the above-mentioned control on the formation of our desired nano-architecture. Meanwhile, the resulting Ni atoms dispersed on the MoO_x nanosheets serve as the active sites for the depositing NiMo alloy from the Ni²⁺ and MoO₄²⁻ ions, ultimately forming the Ni₄Mo nanoparticles on the nanosheets (for the reaction formula, please refer to SI).

Scanning electron microscopy (SEM) image of the Ni₄Mo/MoO_x grown on Cu foam is shown in **Figure S2**. It can be seen that the electrodeposited Ni₄Mo/MoO_x catalyst displays an atypical nanosheet morphology. Unlike a regular nanosheet array, the ultrathin nanosheets curve and fold, exhibiting a nanoflower structure on a large scale. Meanwhile, the nanosheets are assembled close together and uniformly distributed on the substrate, forming a well-connected three-dimensional framework. The structure was further studied by transmission electron microscopy (TEM). **Figure 1B** clearly shows the ultrathin nanosheet morphology of the as-synthesized catalyst, in accord with the structure discovered in the SEM images above, and the thickness of MoO_x nanosheet is about 2.3 nm as shown in the enlarged image (the inset). By zooming in more closely, we observed many homogeneously distributed nanoparticles with a diameter of about 5 nm on average on the nanosheets (**Figure 1C and Figure S3**). High-resolution TEM shows lattice fringes of (121) and (310) planes of the Ni₄Mo nanoparticle, which correspond to d values of 0.207 and 0.180 nm, respectively (**Figure 1D**). No crystal

lattice of MoO_x nanosheets could be observed in TEM images, confirming that the nanosheets are in the amorphous state. The selective area electron diffraction (SAED) pattern (**Figure 1E**) also evidences the existence of Ni₄Mo nanoparticles. Namely, the strong inner diffraction ring could be indexed to (121) plane of Ni₄Mo, and the weaker outer ring corresponds to the (312) plane. The bright (121) plane diffraction ring suggests that most of the facet exposed is (121), and the corresponding lattice is exactly what we observed most frequently in high-resolution TEM images. Additionally, no MoO_x diffraction dots could be found in the SAED pattern, again indicating the amorphous nature of the nanosheets. The energy dispersive X-ray (EDX) elemental mapping (**Figure 1F**) confirms the uniform distribution of Ni, Mo, and O with a Ni/Mo ratio of ~ 2.8:1 (**Figure S4**).

The catalysts were sonicated off the Cu foam to a suspension, which was then cast onto a glass plate for XRD characterization to avoid the strong interference of substrate peaks. The X-ray diffraction (XRD) pattern of Ni₄Mo/MoO_x is shown in **Figure S5**. A small peak at around 43° was observed, supporting the formation of Ni₄Mo nanoparticles. Further information about the composition of the electrocatalyst was obtained from Raman spectroscopy. The strong Raman peaks presented in the range of 550-1000 cm⁻¹ (**Figure 2A**) are typical of amorphous molybdenum oxide, and the amorphous nature explains why the MoO_x phase evaded the aforementioned XRD detection. Specifically, the broadband starting from 550 to 800 cm⁻¹ is ascribed to the triply coordinated oxygen (Mo₃-O), the second peak at about 842 cm⁻¹ represents the doubly coordinated oxygen stretching mode (Mo₂-O), and the last wide peak ranging from 890-980 cm⁻¹ could be attributed to the terminal Mo=O stretching vibration. Compared with the Raman spectra reported previously by other groups, the slight peak shift is possibly caused by the electronic interactions between MoO_x and other components of the catalyst which would change the vibration frequencies of the O-Mo bonds.

To verify the presence of Ni, Mo, and O in the Ni₄Mo/MoO_x electrocatalyst, we resorted to X-ray photoelectron spectroscopy (XPS), see the survey spectrum in **Figure 2B**. The high-resolution Ni 2p XPS spectrum (**Figure 2C**) shows the characteristic peaks of Ni⁰ (pink curves) and Ni²⁺ (orange curves) with two broad shakeup satellites (cyan curves). And the Mo 3d XPS spectrum (**Figure 2D**) could be deconvoluted into eight peaks: four fitted in the Mo 3d_{3/2} region and four in Mo 3d_{5/2} region, indicating the coexistence of Mo⁰ (pink curves), Mo⁴⁺ (wine curves), Mo⁵⁺ (olive curves), and Mo⁶⁺ (gray curves) states. In order to investigate the catalyst without the influence of surface oxidation, we conducted XPS with Ar etch to observe the valence states of each element inside. From **Figure 2E** and **2F**, it is clearly shown that Ni²⁺ were all reduced to Ni⁰, while Mo element exists not only in the form of Mo⁰, but also oxidation forms including Mo⁴⁺ and Mo⁵⁺. And the Ni/Mo ratio was measured to be 3.4:1 (**Table S1**), which further evidences the successful synthesis of Ni₄Mo/MoO_x structure.

The electrochemical characterizations were conducted in 1 M KOH. Hg/HgO, carbon rod, and Cu foam with catalysts were used as a reference, counter, and the working electrode, respectively. **Figure 3A** shows the polarization curves of Pt/C, bare Cu substrate, Ni metal, Ni₄Mo alloy (**Figure S6**), and Ni₄Mo/MoO_x grown on Cu foam for HER electrocatalysis. Pt/C exhibits the lowest overpotential with onset potential near zero. (**Figure 3A**, magenta curve) The bare Cu foam displays very low HER activity, and more than -0.35 V vs. RHE is needed in order to reach a current density of 10 mA/cm² (**Figure 3A**, black curve). Ni metal (**Figure 3A**, olive curve), Ni₄Mo alloy (**Figure 3A**, blue curve) and Ni₄Mo/MoO_x (**Figure 3A**, red curve) exhibit HER overpotential of 169 mV, 40 mV and 16mV, respectively to achieve the same current density. Evidently, the HER activity of Ni increased substantially by forming an alloy with Mo, and the activity is further boosted by constructing the Ni₄Mo/MoO_x nanointerfaces, indicating the beneficial bimetallic ligand effect and synergetic effect of between metal and metal oxide.

The Tafel slope was measured to characterize the HER kinetics. By fitting linear part of Tafel plot, the Tafel slope of Ni₄Mo/MoO_x was determined to be 64 mV/dec, much smaller than 95 mV/dec, 140 mV/dec, and 190 mV/dec of Ni, Ni₄Mo alloy, and bare Cu foam, respectively (**Figure 3B**). The Tafel slope of Ni₄Mo/MoO_x lies in the range of 40-120 mV/dec, indicating that the water dissociation is induced by charge-transfer process featuring the kinetics of both the Volmer step ($\text{H}_2\text{O} + \text{e}^- \rightarrow \text{H}_{\text{ad}} + \text{OH}^-$) and the Heyrovsky step ($\text{H}_2\text{O} + \text{e}^- + \text{H}_{\text{ad}} \rightarrow \text{H}_2 + \text{OH}^-$). The superior electrode reaction kinetics of Ni₄Mo/MoO_x was further exposed by electrochemical impedance spectroscopy (EIS). Ni₄Mo alloy and Ni₄Mo/MoO_x shows much lower charge transfer resistance (R_{ct}) compared with Ni and bare Cu foam as shown in **Figure 3C**. Meanwhile, the R_{ct} of Ni₄Mo/MoO_x (3.7 Ω) is almost half of the R_{ct} of Ni₄Mo alloy (6.9 Ω) at an overpotential of 130 mV, confirming the quicker water dissociation process and the faster HER kinetics of Ni₄Mo/MoO_x. Long-term stability of Cu-support Ni₄Mo/MoO_x was tested via chronopotentiometry. The potential required to reach high current densities of 10 mA/cm², 50 mA/cm², and 100 mA/cm² all showed a slight decline after 24-hours of operation (**Figure 3D**), see the polarization curve after chronopotentiometry measurement in **Figure S7**. The hydrogen production rate and stability test of Cu-supported Ni₄Mo/MoO_x in 30% KOH at 70 °C refer to **Figure S8-11**.

Our integrated design of multi-component HER electrocatalyst targets two central kinetic aspects simultaneously: the water dissociation step and the hydrogen adsorption/desorption step. As we know, one of the most important reasons causing the sluggish HER kinetics in alkaline solution is the weak interaction between water and catalyst surface, making the initial water adsorption step difficult on account of the high dissociation energy barrier of water on the catalyst surface.^[13] This is distinct from the HER process in an acidic environment, which involves proton as the reactant.^[14] To optimize the water dissociation step, the first thing we

considered is to construct metal/metal oxide nanointerfaces. Generally speaking, metal and metal oxide could manifest a synergetic effect at the interface, in which the interface assists in the heterolytic splitting of water into H^+ and OH^- , and afterward, metal oxide helps to attract the OH^- generated during water dissociation, avoiding the block of metal active sites.^[8b, 15] Thus, constructing Ni_4Mo and MoO_x interfaces are highly desirable. Moreover, the more nanointerfaces exposed to the electrolyte, the better the HER performance is expected. So our effort to tune the size of Ni_4Mo nanoparticles on MoO_x nanosheets helped to optimize the number of exposed nanointerfaces and contributed to the HER performance enhancement.

In order to increase the Ni_4Mo/MoO_x nanointerfaces exposed to the electrolyte, we tuned the size of Ni_4Mo nanoparticles on MoO_x nanosheets by controlling the precursor concentration in electrodeposition solution. The nucleation and growth rate of alloy could be controlled by the concentration of each component in the precursor solution and thus helps to tune the particle size in Ni_4Mo/MoO_x structure. (For more details, please refer to SI) In **Figure 4**, Ni_4Mo nanoparticle diameters from 3 nm (**Figure 4A, D**), 5 nm (**Figure 4B, E**), to 7 nm (**Figure 4C, F**) on average are demonstrated with one TEM image in large scale and one in small scale. The red dashed circles marked in the TEM images show the typical Ni_4Mo nanoparticles with different sizes, and we could clearly observe the continuous Ni_4Mo crystal lattice of these nanoparticles. According to the TEM images, the Ni_4Mo nanoparticles with an average size of 5 nm showed a higher proportion of nanointerfaces, and the corresponding electrochemical property test proved to exhibit the highest HER catalytic activity (**Figure S12**).

The second thing we consider is then the adsorption/desorption energy of hydrogen on the surface of the electrocatalyst. This could be discussed together with another critical criterion, i.e., how to optimize the water adsorption because both of these problems could be related to the electronic structure modification. First, the H atom in water molecule is electron-deficient

and thus tends to interact strongly with electron-rich active sites, leading to the down-shift of water adsorption energy. So electron-rich active site is beneficial for water adsorption step.^[13a] Second, from the volcano plot, both Ni and Mo locate at the left side, indicating these two elements exhibit strong adsorption toward hydrogen.^[16] The hybridization of metal d-orbital with adsorbed H orbital gives rise to a low-energy bonding orbital (σ) and a high-energy anti-bonding orbital (σ^*), in which the σ is fully filled while the σ^* is partially filled. It means that the filling of σ^* determines the bonding strength between metal and H.^[17] Drawing on this theory, down-shift of the d-band center will lead to an increment of σ^* occupancy by descending the σ^* level, thus weakening the adsorption energy of H*.^[18] So if we could modify the electron structure of Ni₄Mo/MoO_x by creating Ni₄Mo electron-rich active sites, on one hand, it could facilitate the water adsorption by forming stronger interaction with electron-deficient H in water molecule. On the other hand, it is possible to optimize the H desorption process through lowering the d band energy. As we know, the electronegativity of Ni (1.92) and Mo (2.16) is relatively higher than Cu (1.90), thus, the Ni₄Mo/MoO_x thin film supported on Cu at interface area may possibly become more electron-rich than the same catalyst grown on Ni. Pursuing this conception, Cu foam was chosen as the substrate instead of commonly used Ni foam.

The conductivity difference between bare Ni foam and Cu foam was excluded by the conductivity test (**Figure S13, Table S2**). We further collected the XPS profile of Cu with different Ar etch depth to investigate the influence of Cu substrate to the electrocatalyst thin film. According to **Figure 5A**, the intensity of Cu peak increases as we detect areas closer to the substrate, indicating Cu potentially diffused into the Ni₄Mo/MoO_x structure, and affect the catalytic activity of the supported catalyst by changing the Ni₄Mo/MoO_x local environment. Meanwhile, the structure prepared by electrodeposition is electrolyte-permeable so that the

underlying Cu interfacial sites could be exposed as active sites.^[19] The influence of Cu substrate to the catalyst is verified by XPS and UPS. The binding energy of both Ni and Mo exhibit a hypsochromic shift when Ni₄Mo/MoO_x was loaded on Cu substrate (**Figure 5B** and **5C**), and the maximum values of valence band for catalyst on Ni and Cu substrate were measured to be ~2.81 eV and ~3.08 eV respectively, indicating a downshift of valence band that away from Fermi level using Cu as substrate (**Figure S14**). The structure and HER performance of Ni₄Mo/MoO_x with different metal supports are demonstrated in **Figure S15-16**. Ni-based catalyst supported on Cu substrate displays higher HER activity than the same catalyst loaded on Ni substrate, reflecting in the clear decrease of overpotential in 1 M KOH (**Figure 5D**). A detailed comparison of our electrocatalyst with reported works also confirms the superior performance of our nanointerface systems (**Table S3**).

To shed more light on the HER mechanism, we have conducted a model study on the electronic properties and energetics of the interface simply built from Ni₄Mo and MoO_x. We start from the Ni₄Mo/MoO_x interface, which displays a strong bonding between the Ni₄Mo and MoO_x with clear distortion with varied coordination numbers. The electronic distribution indicates a semi-metallic feature based on electron-rich Ni sites and hole-rich O sites (**Figure 6A**). Similarly, this Cu-substrate supported interface system also presents a semi-metallic electronic conducting behavior. However, the electronic distribution indicates that Ni-Mo alloy dot turns to be electron-rich area and even performs a local connected electron-rich network between the nearest neighboring Ni-Mo alloy dot (**Figure 6B**). From the detailed projected partial density of states (PDOS), we found that the 3d-band of the Ni-site at the interface has been suppressed and downshifted about 1.9 eV from the change of peak-to-peak when compared to bulk (**Figure 6C**). In contrast, the electronic activities of Mo-sites at the interface region have been largely boosted-up to close position near Fermi level (E_F) (**Figure 6D**). Turning to the electronic properties of the model, we found the 3d-band arising from the on-site Ni-3d orbital levels has

been modulated into three different regions based on the PDOSs calculations (**Figure 6E**). The bulk metal Ni-3d band occupies the highest level next to the E_F , i.e., $E_V-0.7$ eV ($E_V=0$ for E_F), only 0.7 eV below E_F . When the Ni-site is in the $Ni_4Mo||MoO_x$ and $Ni_4Mo||MoO_x||Cu$ systems, however, the 3d-band center has been further shifted to a lower level at $E_V-1.3$ eV and $E_V-2.5$ eV, respectively. The shifting takes place because the electron-rich effect turns to be more and more obvious and the Coulomb repulsive on-site potential will further suppress the electronic occupying states for downshifting toward lower energy levels. Thus, the evolution of the 3d-band center is such that the deepest 3d-band center turns out to be the Ni-site located within the $Ni_4Mo||MoO_x||Cu$ model system. This indicates that with the assistance of the Cu-substrate support, the catalyst active site (Ni-Mo alloy dot) will be even more electron-rich. For the MoO_x constituent (**Figure 6F**), the deep localized O-2p band further boosted-up the charge transfer by the effective binding of the O-related species. This arises because the O-2p orbital substantially overlaps with the Mo-4d- t_{2g} state propelling more electrons towards the Mo-4d- e_g level as 4d-electron rich center nearby the E_F . This trend leads the Mo-sites to high binding activities for accommodating p-electrons of [$*OH^-$] group. Overall, the interface region of the $Ni_4Mo||MoO_x$ system provides a high activity for bond-cleavage of water-splitting and guarantees the HER performance under the alkaline condition.

The free energy profile for the HER pathway under the alkaline condition for Cu-substrate supported interface system has been also studied based on the consideration of ΔG with zero-point energy (ZPE). Overall, the $Ni_4Mo||MoO_x$ interface model shows substantial energetic favorable with reaction energy (-1.35 eV) gained for the HER. The initial activation is proceeded by energetic preferred water splitting effect ($H_2O^*+H^*\rightarrow HO^*+2H^*$) with energy of -1.25 eV lowered. Moreover, there seems to be no obvious energy difference (~ 0.1 eV) for the following step of $2H^*\rightarrow H_2\uparrow$ (**Figure 7A**). In comparison, another $Ni_4Mo||MoO_x$ interface model based on smaller bonding density of Ni-O shows a similar physicochemical trend with

the slightly smaller overall released reaction heat (-1.15 eV). The only difference is exhibited at the step of the water-splitting process to activate the whole HER process. This step turns to be 0.51 eV higher than the interface model with larger oxygen bonding density (**Figure 7B**). The water splitting induces more energy gain for the Ni₄Mo||MoO_x||Cu system due to the stronger bonding of the Mo-(OH). Therefore, the initial activation proceeds by energetically preferred water splitting effect ($\text{H}_2\text{O}^* + \text{H}^* \rightarrow \text{HO}^* + 2\text{H}^*$) with energy level of -3.00 eV. Moreover, there seems to be almost 1 eV further energetic drop for the following step of $2\text{H}^* \rightarrow \text{H}_2\uparrow$. This might indicate the HER reaction rate under alkaline condition catalyzed by this interface system is fast and efficient for generation and desorption of H₂ (**Figure 7C**). The chemisorption energies also consistently indicate good HER performance (**Figure 7D**). The H-chemisorption energy is -0.35 eV below the thermoneutral line ($\Delta G=0$), which can be stably adsorbed without too high a binding energy. On the other hand, the H₂-desorption shows a very clear desorption behavior with 0.13 eV higher than the thermoneutral line. We also found that the water splitting at the interface is potentially very efficient since the energy contrast shows the process of $\text{H}_2\text{O}^* \rightarrow \text{H}^* + \text{OH}^*$ prefers to take place at the interface region (**Figure 7E**). Therefore, we finally confirm that the interface region of the Ni₄Mo||MoO_x system is indeed the most catalytically active site for highly efficient HER under alkaline condition. Therefore, we finally confirm the interface region of Ni||MoO_x system can be a good catalytic area for highly efficient HER under the alkaline condition. Therefore, the activities of 4d-band of Mo can be promoted by Ni-3d orbital Coulomb interaction and being highly active for charge exchange with protons. The synergetic effect between Ni and Mo enables the cell model towards efficient HER is summarized in **Figure 7F**.

In an effort to create multi-component HER electrocatalyst in a scalable fashion by integrated design, we have successfully synthesized Cu-supported Ni₄Mo nanodot on MoO_x ultrathin nanosheet via a one-step electrodeposition process. The as-obtained catalyst shows an

overpotential of 16 mV at the current density of 10 mA/cm² in 1M KOH, and 105 mV to achieve a current density of 2500 A/m² in 70 °C 30% KOH, proving the excellent HER activity of the catalyst in alkaline media. More concretely, the following features are beneficial for the superior HER activity of Cu-supported Ni₄Mo/MoO_x: 1) The reaction route was optimized through elaborating the Ni₄Mo/MoO_x nanointerfaces, 2) The Ni₄Mo/MoO_x nanointerfaces exposed to the electrolyte was maximized by controlling the Ni₄Mo nanoparticle size, and 3) The mutual modulation of d-band by Ni and Mo provides a synergetic effect for being a micro-cathode towards efficient proton-electron charge exchange. This work supplies a key explanation for the high HER performance of a series of transition metal/ metal oxide catalyst, especially in alkaline media, which is pivotal for future electrocatalyst design and fabrication.

Acknowledgments

The authors acknowledge the financial support of this work from the NFSC/Hong Kong RGC Research Scheme (N_HKUST610/14), the RGC of Hong Kong (GRF Nos. 16312216 and 16300915), the Early Career Scheme (ECS) fund (Grant No.: PolyU 253026/16P) from the RGC of Hong Kong, the Shenzhen Peacock Plan (KQTD2016053015544057), and the National Science Foundation of China (contract number 21703003, 21771156). The author also acknowledges the discussion with M. Sun and T. Wu.

Received: ((will be filled in by the editorial staff))

Revised: ((will be filled in by the editorial staff))

Published online: ((will be filled in by the editorial staff))

References

- [1] I. Roger, M. A. Shipman, M. D. Symes, *Nature Reviews Chemistry* **2017**, *1*, 0003.
- [2] T. R. Cook, D. K. Dogutan, S. Y. Reece, Y. Surendranath, T. S. Teets, D. G. Nocera, *Chemical reviews* **2010**, *110*, 6474-6502.
- [3] H. B. Gray, *Nature chemistry* **2009**, *1*, 7.
- [4] W. Sheng, H. A. Gasteiger, Y. Shao-Horn, *Journal of The Electrochemical Society* **2010**, *157*, B1529-B1536.
- [5] J. Wang, F. Xu, H. Jin, Y. Chen, Y. Wang, *Advanced Materials* **2017**, *29*, 1605838.

- [6] a) N. Danilovic, R. Subbaraman, D. Strmcnik, K. C. Chang, A. Paulikas, V. Stamenkovic, N. M. Markovic, *Angewandte Chemie* **2012**, *124*, 12663-12666; b) K. Zeng, D. Zhang, *Progress in Energy and Combustion Science* **2010**, *36*, 307-326.
- [7] a) M. Dresselhaus, I. Thomas, *Nature* **2001**, *414*, 332; b) N. S. Lewis, D. G. Nocera, *Proceedings of the National Academy of Sciences* **2006**, *103*, 15729-15735.
- [8] a) M. Gong, W. Zhou, M.-C. Tsai, J. Zhou, M. Guan, M.-C. Lin, B. Zhang, Y. Hu, D.-Y. Wang, J. Yang, *Nature communications* **2014**, *5*, 4695; b) M. Gong, D.-Y. Wang, C.-C. Chen, B.-J. Hwang, H. Dai, *Nano Research* **2016**, *9*, 28-46; c) M. Janjua, R. Le Roy, *International Journal of Hydrogen Energy* **1985**, *10*, 11-19.
- [9] a) Y. Y. Chen, Y. Zhang, X. Zhang, T. Tang, H. Luo, S. Niu, Z. H. Dai, L. J. Wan, J. S. Hu, *Advanced Materials* **2017**, *29*, 1703311; b) M. Fang, W. Gao, G. Dong, Z. Xia, S. Yip, Y. Qin, Y. Qu, J. C. Ho, *Nano Energy* **2016**, *27*, 247-254; c) X. Long, H. Lin, D. Zhou, Y. An, S. Yang, *ACS Energy Letters* **2018**, *3*, 290-296; d) J. Zhang, T. Wang, P. Liu, Z. Liao, S. Liu, X. Zhuang, M. Chen, E. Zschech, X. Feng, *Nature communications* **2017**, *8*, 15437.
- [10] a) I. A. Raj, K. Vasu, *Journal of applied electrochemistry* **1990**, *20*, 32-38; b) I. A. Raj, K. Vasu, *Journal of applied electrochemistry* **1992**, *22*, 471-477.
- [11] a) Y. Jin, H. Wang, J. Li, X. Yue, Y. Han, P. K. Shen, Y. Cui, *Advanced Materials* **2016**, *28*, 3785-3790; b) Z. Luo, R. Miao, T. D. Huan, I. M. Mosa, A. S. Poyraz, W. Zhong, J. E. Cloud, D. A. Kriz, S. Thanneeru, J. He, *Advanced Energy Materials* **2016**, *6*, 1600528.
- [12] a) Y. Wang, G. Zhang, W. Xu, P. Wan, Z. Lu, Y. Li, X. Sun, *ChemElectroChem* **2014**, *1*, 1138-1144; b) J. R. McKone, B. F. Sadler, C. A. Werlang, N. S. Lewis, H. B. Gray, *ACS Catalysis* **2013**, *3*, 166-169.
- [13] a) B. You, X. Liu, G. Hu, S. Gul, J. Yano, D.-e. Jiang, Y. Sun, *Journal of the American Chemical Society* **2017**, *139*, 12283-12290; b) Y. Zheng, Y. Jiao, M. Jaroniec, S. Z. Qiao, *Angewandte Chemie International Edition* **2015**, *54*, 52-65.

- [14] Y. Jiao, Y. Zheng, M. Jaroniec, S. Z. Qiao, *Chemical Society Reviews* **2015**, *44*, 2060-2086.
- [15] R. Subbaraman, D. Tripkovic, D. Strmcnik, K.-C. Chang, M. Uchimura, A. P. Paulikas, V. Stamenkovic, N. M. Markovic, *Science* **2011**, *334*, 1256-1260.
- [16] Y. Zheng, Y. Jiao, Y. Zhu, L. H. Li, Y. Han, Y. Chen, A. Du, M. Jaroniec, S. Z. Qiao, *Nature communications* **2014**, *5*, 3783.
- [17] a) B. Hammer, J. Nørskov, *Surface Science* **1995**, *343*, 211-220; b) J. R. Kitchin, J. K. Nørskov, M. A. Barteau, J. Chen, *Physical review letters* **2004**, *93*, 156801.
- [18] J. Greeley, T. F. Jaramillo, J. Bonde, I. Chorkendorff, J. K. Nørskov, in *Materials For Sustainable Energy: A Collection of Peer-Reviewed Research and Review Articles from Nature Publishing Group*, World Scientific, **2011**, pp. 280-284.
- [19] a) M. S. Burke, M. G. Kast, L. Trotochaud, A. M. Smith, S. W. Boettcher, *Journal of the American Chemical Society* **2015**, *137*, 3638-3648; b) S. Zou, M. S. Burke, M. G. Kast, J. Fan, N. Danilovic, S. W. Boettcher, *Chemistry of Materials* **2015**, *27*, 8011-8020.

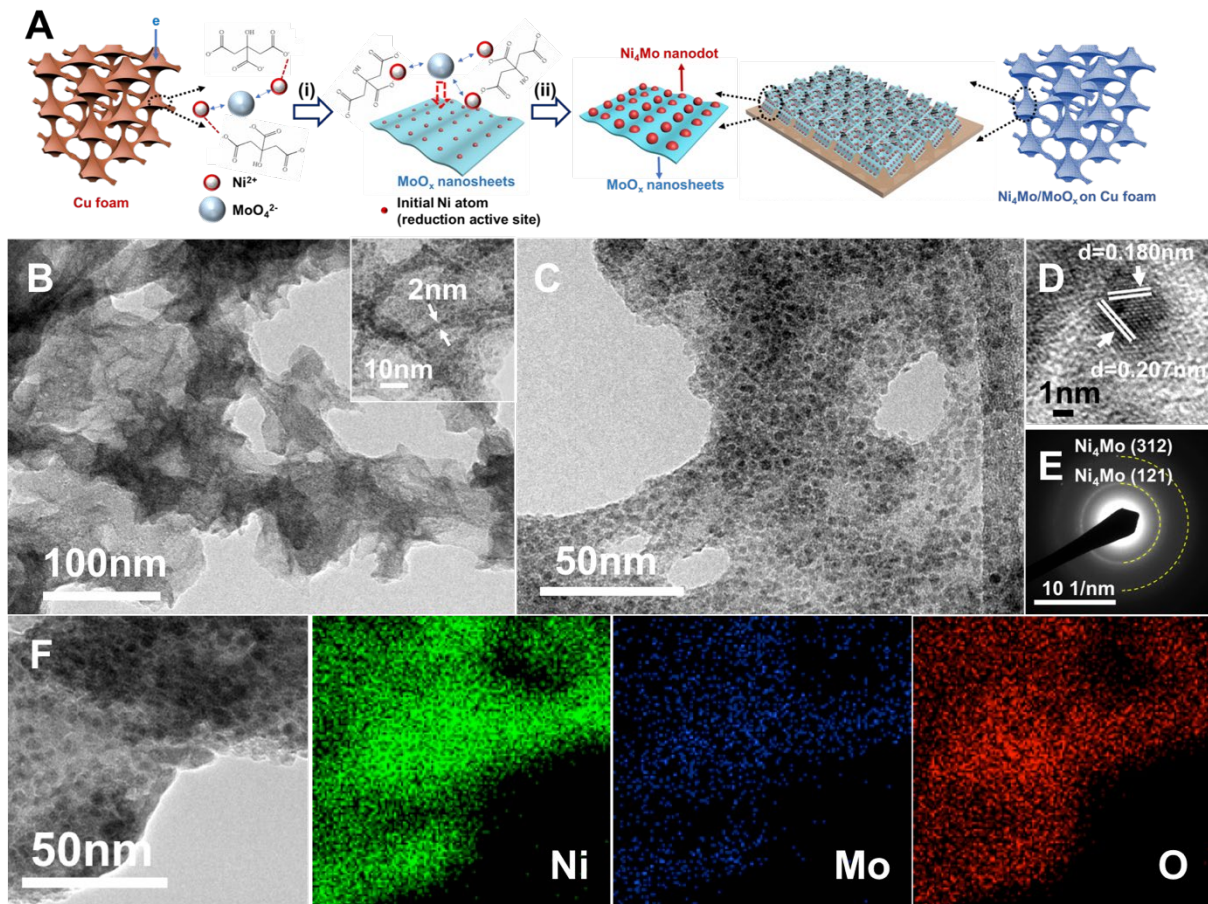


Figure 1. A) Schematic of the $\text{Ni}_4\text{Mo}/\text{MoO}_x$ synthesis route in Cu foam. (i) induced co-deposition; (ii) formation of nanointerfaces with the dispersion of the alloy nanoparticles. Microscopic morphology and structure characterizations of $\text{Ni}_4\text{Mo}/\text{MoO}_x$; B,C) TEM images; D) HRTEM image; E) SAED pattern and F) EDX elemental mapping of Ni_4Mo nanoparticle on amorphous MoO_x nanosheet.

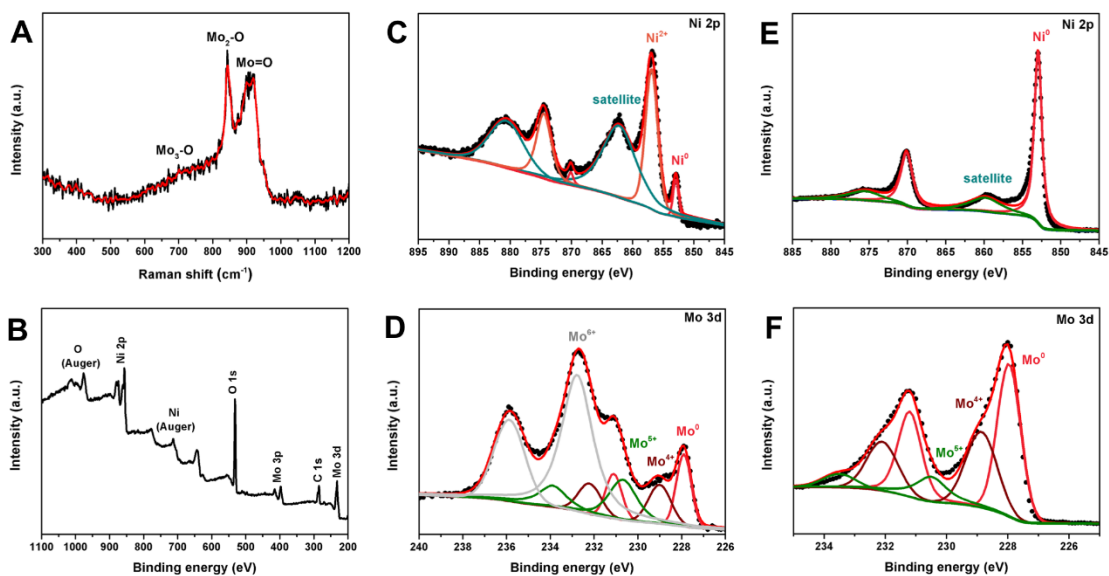


Figure 2. Spectroscopic characterizations of $\text{Ni}_4\text{Mo}/\text{MoO}_x$. A) Raman spectra; B) XPS survey spectrum; High-resolution XPS spectra on C) Ni 2p, D) Mo 3d of the as-prepared sample; High-resolution XPS spectra on E) Ni 2p, F) Mo 3d after Ar sputtering for 130 s.

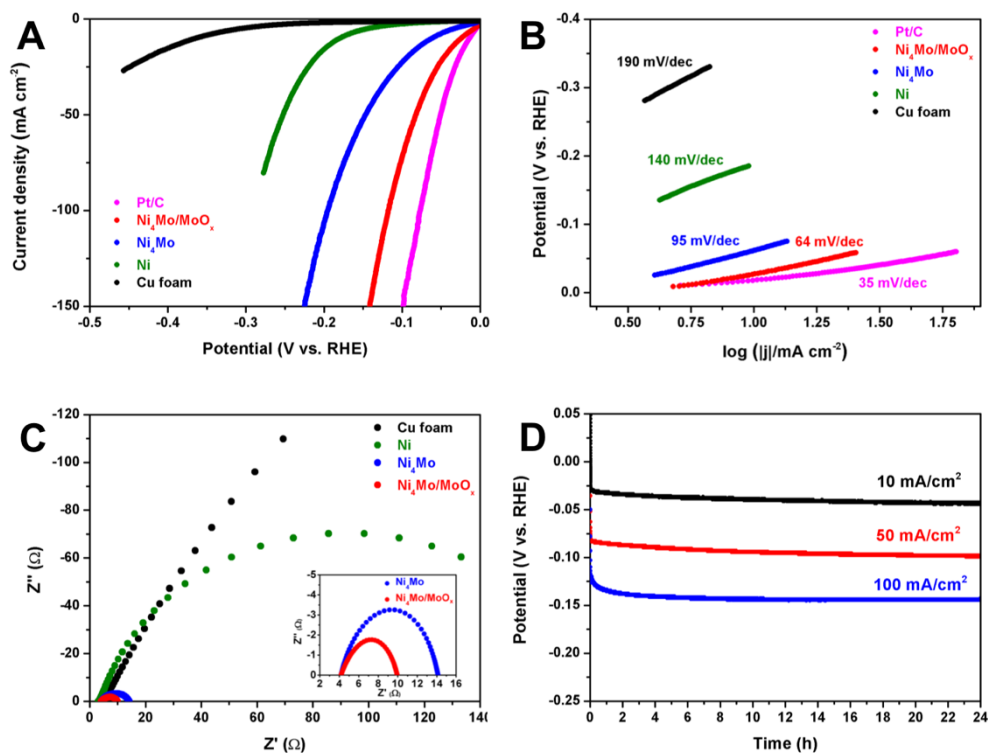


Figure 3. Electrochemical characterizations of Pt/C, bare Cu foam, Ni, Ni₄Mo alloy, and Ni₄Mo/MoO_x. A) LSV curves; B) Tafel plots and C) EIS; D) long-term stability tests of Ni₄Mo/MoO_x.

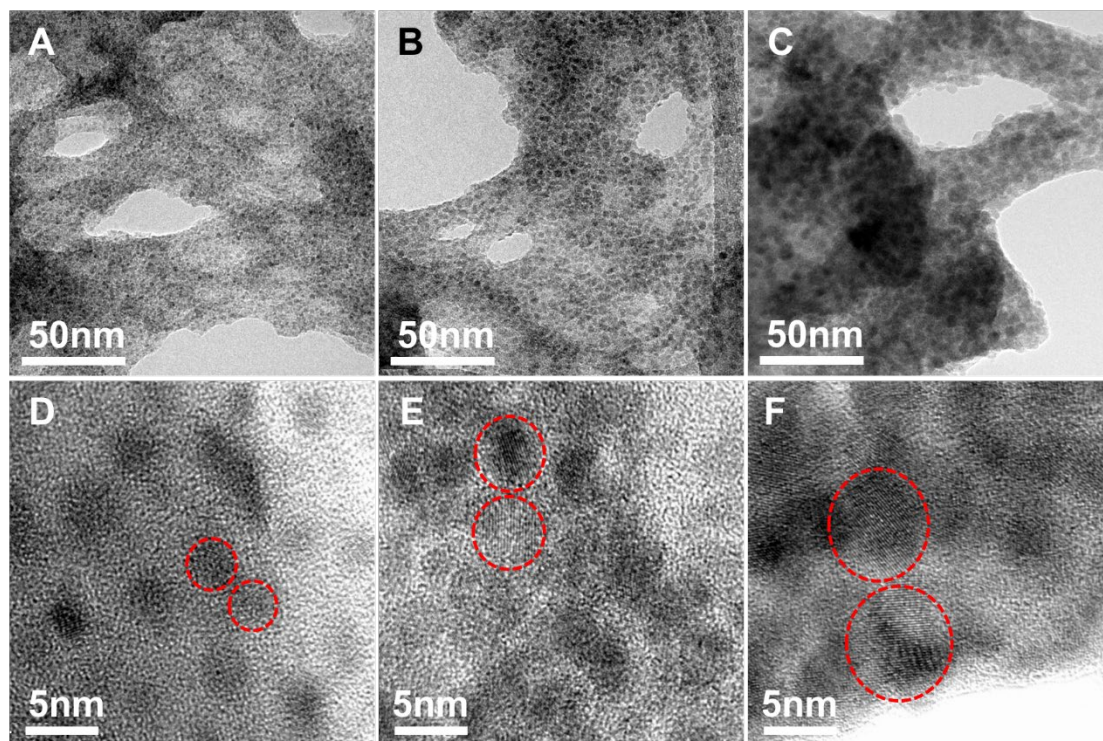


Figure 4. TEM images of Ni₄Mo/MoO_x with different Ni₄Mo nanoparticle sizes. The average Ni₄Mo nanoparticle diameter of A,D) 3 nm; B,E) 5 nm and C,F) 7 nm.

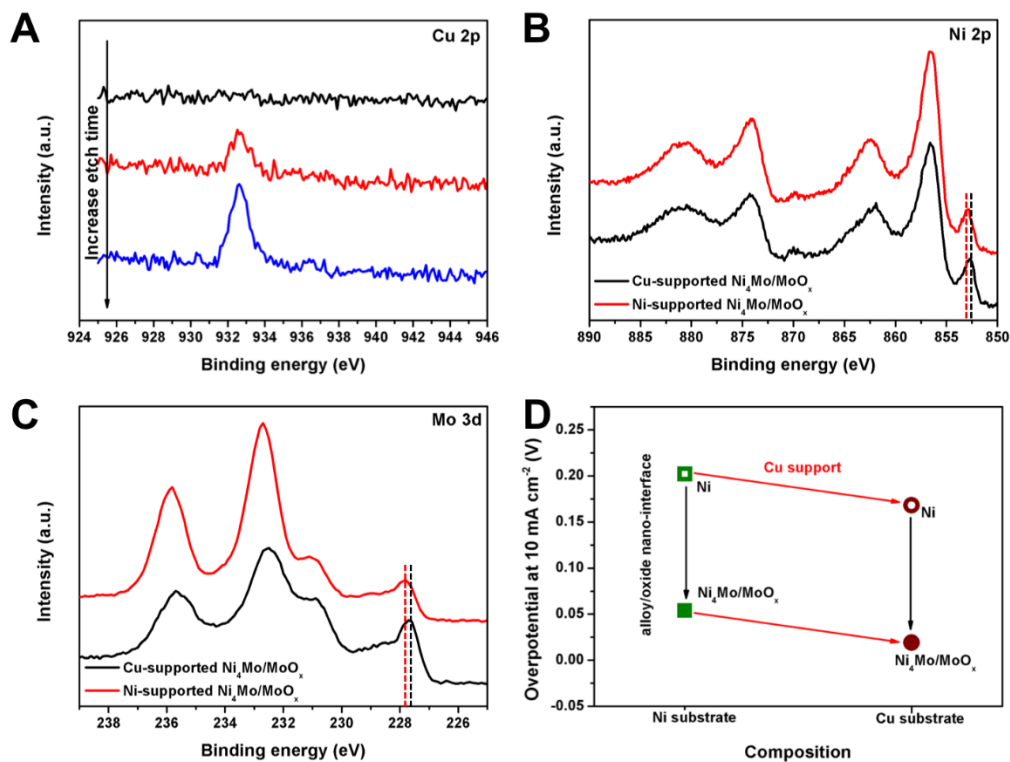


Figure 5. A) XPS Cu 2p depth profile of Cu-supported Ni₄Mo/MoO_x with 0s (black), 130s (red), and 390s (blue) Ar sputters; Cu-supported and Ni-supported Ni₄Mo/MoO_x XPS spectra of B) Ni 2p and C) Mo 3d; D) overpotential of electrocatalysts supported on Ni substrate and Cu substrate.

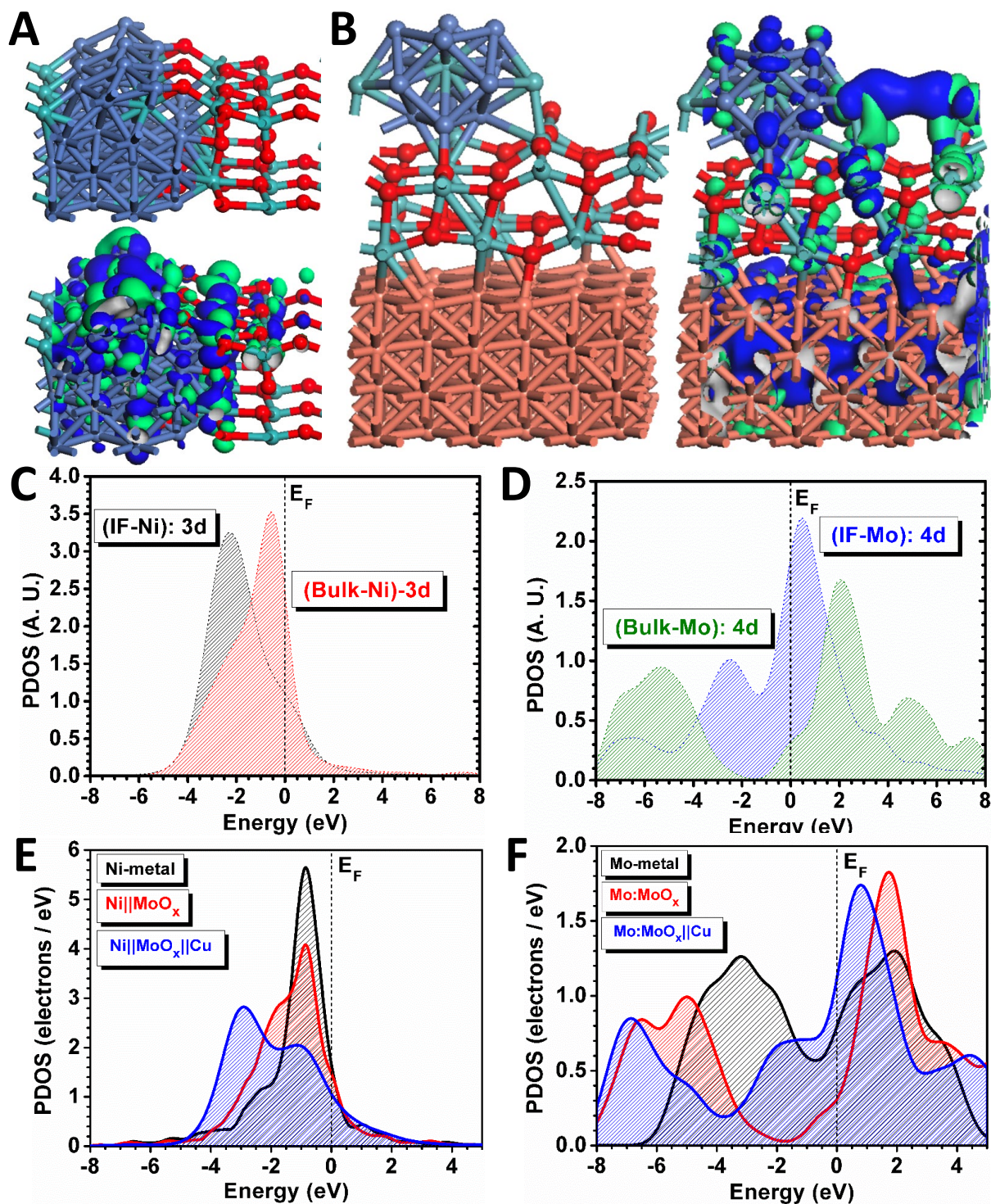


Figure 6. Electronic properties of interface model systems. The local atomic view and 3D orbital contour of the HOMO (blue) and LUMO (green) near the A) Ni||MoO_x interface and B) Ni||MoO_x||Cu interface. Brown balls = Cu; Cyan balls = Mo; Blue balls = Ni; and Red balls = O. C) The PDOSs of the Ni-3d band of the bulk and the one-interface and the two-interface model structures. D) The PDOSs of the Mo-4d band of the bulk and the one-interface and the two-interface model structures. E) The PDOSs of the Ni-3d band between bulk and interface regions. F) The PDOSs of the Mo-4d band between bulk and interface regions, respectively.

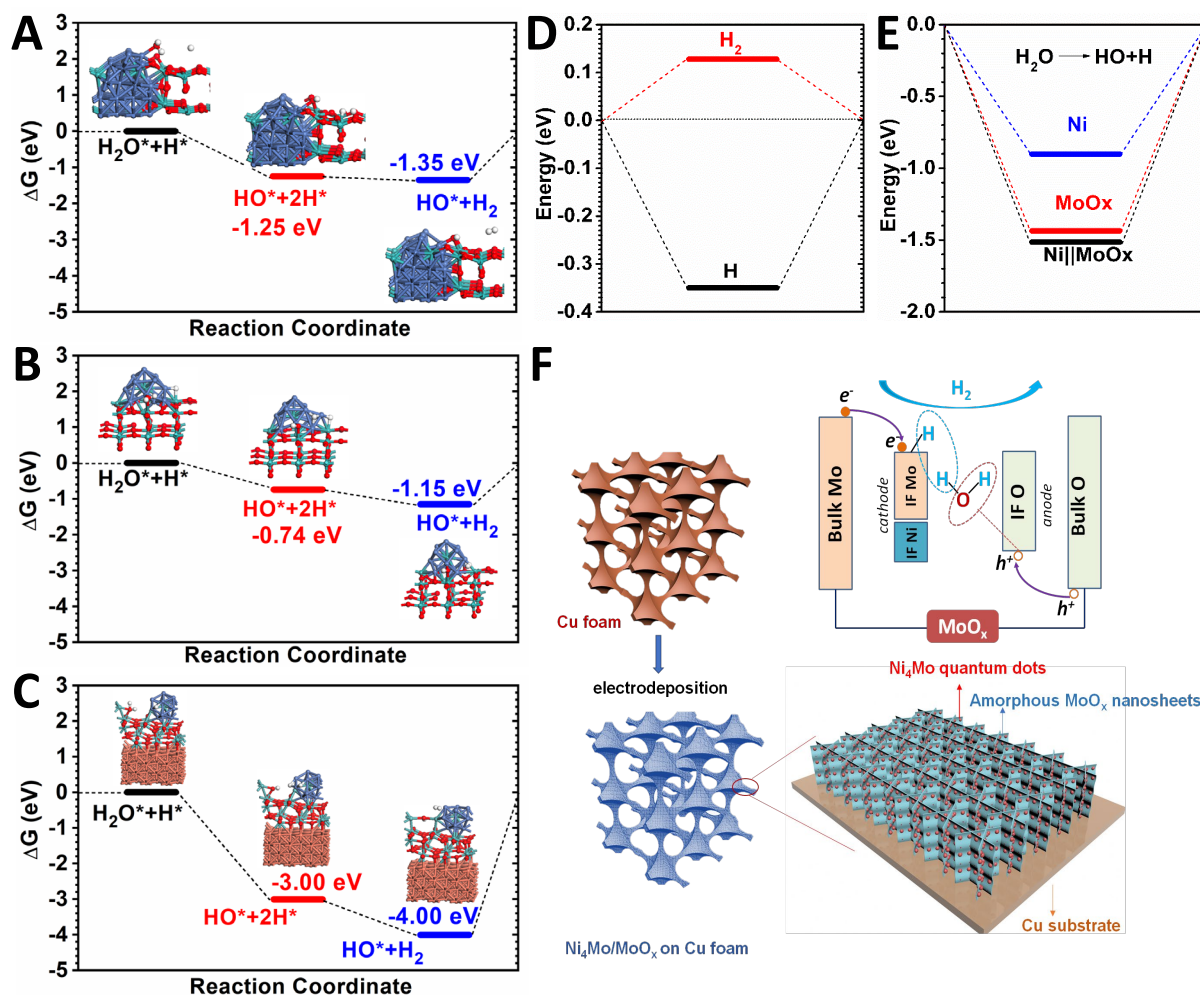


Figure 7. Free energetic pathway, chemisorption, and formation energy for the HER. The reaction pathway for the HER under the alkaline condition is given by the interface with A) more oxidation sites, B) fewer oxidation sites and C) with Cu substrate. D) The chemisorption energy of the H and H_2 at the interface region. E) The formation energy of the water splitting at three different regions of the interface model. F) Schematic Diagram of the HER boosting mechanism by $Ni||MoO_x||Cu$ interface system under the alkaline condition.

The one-step facile synthesis of $\text{Ni}_4\text{Mo}/\text{MoO}_x/\text{Cu}$ heterostructural catalyst. The activities of 4d-band of Mo can be promoted by Ni-3d orbital Coulomb interaction and being highly active for charge exchange with protons to guarantee the efficient HER performance in alkaline media.

Keyword nanointerface, one-step synthesis, d-band structure, NiMo, hydrogen evolution reaction

Yiming An, Xia Long, Ming Ma, Jue Hu, He Lin, Dan Zhou, Zheng Xing, Bolong Huang*, Shihe Yang*

Title: One-step controllable synthesis of $\text{Ni}_4\text{Mo}/\text{MoO}_x/\text{Cu}$ nanointerfaces for highly efficient water reduction

